

Physical Properties of Candidate X-Ray Detector

Material $\text{Rb}_4\text{Ag}_2\text{BiBr}_9$

Zheng Zhang^a, Ying-Zhong Ma^b, Leonard Thomas^a, Krzysztof Gofryk^c, Bayram Saparov^{a*}

^aDepartment of Chemistry & Biochemistry, University of Oklahoma, Norman, Oklahoma 73019,
United States

^bChemical Sciences Division, Oak Ridge National Laboratory, Oak Ridge, Tennessee 37831,
United States

^cIdaho National Laboratory, Idaho Falls, Idaho 83415, United States

*Author to whom correspondence should be addressed: saparov@ou.edu

Recently, metal halide perovskites have emerged as promising semiconductor candidates for sensitive X-ray photon detection due to their suitable bandgap energies, excellent charge transport properties, and low material cost afforded by their low-temperature solution-processing preparation. Here, we report an improved methodology for single crystal (SC) growth, thermal and electrical properties of a two-dimensional (2D) layered halide material $\text{Rb}_4\text{Ag}_2\text{BiBr}_9$, which has been identified as a potential candidate for X-ray radiation detection applications. The measured heat capacity for $\text{Rb}_4\text{Ag}_2\text{BiBr}_9$ implies that there are no structural phase transitions upon cooling. Temperature dependence of thermal transport measurements further suggest remarkably low thermal conductivities of $\text{Rb}_4\text{Ag}_2\text{BiBr}_9$ that are comparable to the lowest reported in literature. The bulk crystal resistivity is determined to be $2.59 \times 10^9 \Omega \cdot \text{cm}$ from the current-voltage (I-V) curve. Density of trap states are estimated to be $\sim 10^{10} \text{ cm}^{-3}$ using the space-charge-limited-current (SCLC) measurements. The fabricated $\text{Rb}_4\text{Ag}_2\text{BiBr}_9$ -based X-ray detector shows good operational stability with no apparent current drift, which may be ascribed to the 2D crystal structure of $\text{Rb}_4\text{Ag}_2\text{BiBr}_9$. Finally, by varying the X-ray tube current to change the corresponding dose rate, the $\text{Rb}_4\text{Ag}_2\text{BiBr}_9$ X-ray detector sensitivity is determined to be $222.03 \text{ uCGy}^{-1}\text{cm}^{-2}$ (at an electric field of $E = 24 \text{ V/mm}$).

■ INTRODUCTION

The detection of X-ray photons plays an important role for a wide range of applications, such as homeland security, medical imaging, nuclear safety monitoring, and scientific research.^{1,2,3} In the past decade, many compound semiconductors have been studied for X-ray photon detection, such as cadmium zinc telluride (CdZnTe or CZT), gallium arsenide (GaAs), and thallium bromide (TlBr).^{4,5,6} CdZnTe

detectors offer the superior energy resolution but suffer from the poor hole transport.⁷ While TlBr is a promising compound semiconductor material, the TlBr detector performance degrades over time due to the charge polarization, which is caused by the bromide anion migration.⁸ Recently, three-dimensional (3D) halide perovskites with the general chemical formula of ABX_3 (where $A = Cs^+$, methylammonium (MA) or formamidinium (FA); $B = Pb^{2+}$; $X = I, Br, Cl$) have emerged as potential next-generation room-temperature X-ray detector materials due to a unique combination of their excellent charge carrier transport properties, suitable bandgap energies (MAPbI₃: 1.57 eV, FAPbI₃: 1.48 eV, CsPbI₃: 1.73 eV)⁹, high semiconductor resistivity ($>10^7 \Omega \cdot cm$) for leakage current reduction, high average atomic number Z for photon attenuation, and low material cost due to their solution processability. Nevertheless, these 3D perovskites also have some drawbacks including the presence of toxic heavy element lead, and their poor stability in ambient air, which is undesirable for their long-term deployment. For example, FAPbI₃ perovskites can undergo facile phase transition from its black polymorph to a yellow phase within a few days when stored in air.¹⁰ To remedy the toxicity and instability issues in 3D halide perovskites, lower-dimensional (i.e., 2D, one-dimensional (1D), and zero-dimensional (0D)) perovskites with larger organic cations, which form moisture resistant layers, have been proposed to replace the 3D halide perovskites.^{11,12}

Among the brand new Pb-free multinary semiconductors that have been recently discovered is $Rb_4Ag_2BiBr_9$, which has a pseudo-2D layered crystal structure. In literature, similar mixed silver-bismuth halides such as Cs_2AgBiX_6 ($X = Cl^-$ or Br^-) have been considered for prospective applications in radiation detection.^{2,29} In fact, $Rb_4Ag_2BiBr_9$ possesses several advantages over the archetypal lead halide perovskites. As reported in our previous work, $Rb_4Ag_2BiBr_9$ has excellent air stability with no decomposition or degradation up to 10 months under ambient air, and good thermal stability with no structural phase transition up to 700 K. Here, we report an improved methodology for growing larger SCs of $Rb_4Ag_2BiBr_9$, which allowed us to evaluate its performance as a potential semiconductor candidate for X-ray radiation detection. Based on heat capacity measurements, $Rb_4Ag_2BiBr_9$ has no structural phase transitions upon cooling. We fabricated $Rb_4Ag_2BiBr_9$ SC-based detector that shows good long-term operation stability with an ideal bulk semiconductor resistivity of $2.59 \times 10^9 \Omega \cdot cm$, and X-ray detector sensitivity of $222.03 \mu CGy^{-1} cm^{-2}$ (at electric field $E = 24 V/mm$). The obtained results on $Rb_4Ag_2BiBr_9$ are discussed together with strategies for further improving the performance of this material for X-ray radiation detection.

■ RESULTS AND DISCUSSION

$Rb_4Ag_2BiBr_9$ was originally discovered through slow evaporation of a stoichiometric solution (aqueous hydrobromic acid was used as a solvent) at $90^\circ C$.¹³ While this technique can produce SCs measuring up to centimeter in size, we further optimized the solution crystal growth method to improve the crystal quality, and to increase the reliability of the preparation method. Based on our most recent results, best quality

$\text{Rb}_4\text{Ag}_2\text{BiBr}_9$ SC growth is achieved by adopting a slow cooling method (Fig. 1a) from 130 °C. The optimized crystal growth methodology produces high quality SCs (Fig. 1b) with dimensions up to $5 \times 4 \times 3$ mm³ within a few hours from the start of the crystal growth. Powder X-ray diffraction (XRD) measurements (Fig. 1c) on ground crystals of $\text{Rb}_4\text{Ag}_2\text{BiBr}_9$ suggest that the optimized method yields pure phase samples without impurity inclusions.



Figure 1. (a) A schematic illustration of the crystal growth process. (b) Photographs of the $\text{Rb}_4\text{Ag}_2\text{BiBr}_9$ SCs. (c) The obtained SCs do not have any impurity inclusions as judged by the comparison of the measured and calculated PXRD patterns of a crushed polycrystalline powder sample of $\text{Rb}_4\text{Ag}_2\text{BiBr}_9$.

The optical bandgap energy of the obtained crystals of $\text{Rb}_4\text{Ag}_2\text{BiBr}_9$ was determined through diffuse reflectance measurements. The diffuse reflectance data plotted as the Kubelka-Munk function $F(R)$ ($= \alpha/S = (1-R)^2/(2R)$, where R is the reflectance, α is the absorption coefficient and S is the scattering coefficient)¹³ against the photon energy is provided in Fig. 2a. The Tauc plots are then calculated (Fig. 2b) based on the Kubelka-Munk function assuming direct and indirect transitions to extract the bandgap energy values of 2.68 eV (direct) and 2.38 eV (indirect) for $\text{Rb}_4\text{Ag}_2\text{BiBr}_9$. These values are consistent with that reported for samples prepared using the slow evaporation technique.¹³ Note that the results of DFT calculations suggest that owing to its low-dimensional crystal structure, $\text{Rb}_4\text{Ag}_2\text{BiBr}_9$ has flat frontier states around the optical band gap leading to slightly indirect nature of its bandgap with a negligible difference of less than 0.01 eV between direct and indirect gaps. Importantly, the measured optical bandgap of $\text{Rb}_4\text{Ag}_2\text{BiBr}_9$ is comparable to the values found for other silver-bismuth halides studied such as $\text{Cs}_2\text{AgBiX}_6$ ($X = \text{Cl}^-$ or Br^-), which have been reported as prospective materials for radiation detection applications.^{2,29}

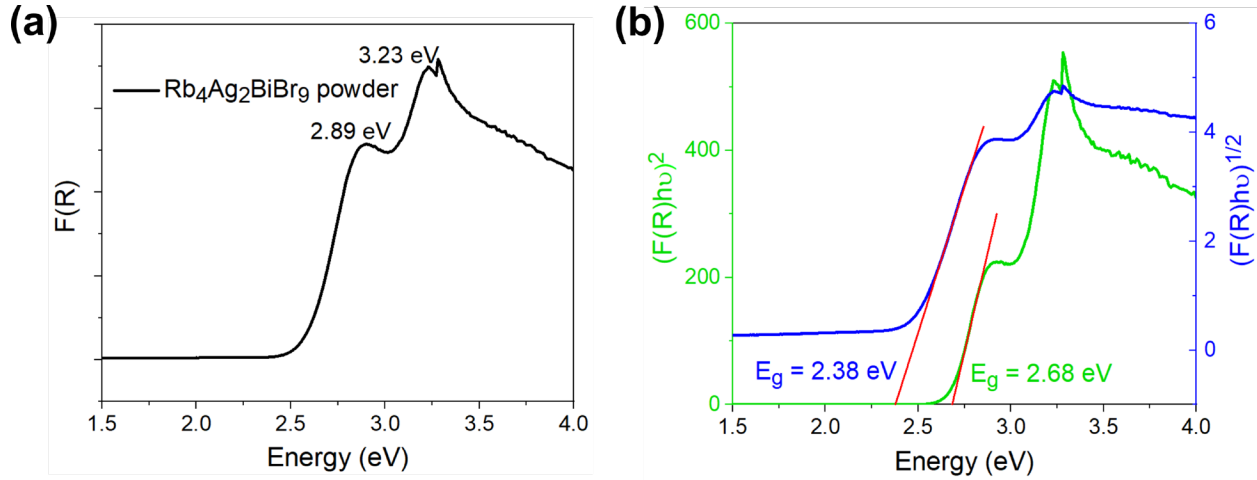


Figure 2. (a) Plot of the diffuse reflectance of $\text{Rb}_4\text{Ag}_2\text{BiBr}_9$ powder as Kubelka-Munk function $F(R)$ against the photon energy. (b) Calculated Tauc plots of $\text{Rb}_4\text{Ag}_2\text{BiBr}_9$ based on the Kubelka-Munk function with assumptions of direct (green) and indirect (blue) transitions.

Hybrid organic-inorganic perovskites can exhibit multiple phase transitions in the vicinity of room temperature, which could present challenges for their implementation in practical applications. To study the thermal properties of $\text{Rb}_4\text{Ag}_2\text{BiBr}_9$, we performed heat capacity and thermal conductivity measurements. **Both properties were measured by using a DynaCool-9 setup (Quantum Design) with HCP and TTP options.** Fig. 3a shows the temperature dependence of the heat capacity of a $\text{Rb}_4\text{Ag}_2\text{BiBr}_9$ SC. The $C_p(T)$ curve exhibits no sign of any phase transitions, **and at high temperatures**, approaches the value expected from the Dulong-Petit law, i.e., $C_p = 3nR = 399.1 \text{ J mol}^{-1}\text{K}^{-1}$, where n is the number of atoms per molecule and R is the gas constant. At low temperatures, the specific heat of $\text{Rb}_4\text{Ag}_2\text{BiBr}_9$ can be well described by the formula: $C_p(T) = \gamma \times T + \beta \times T^3 + \zeta \times T^5$ with the coefficients $\gamma = -0.05 \text{ mJ/mol K}^2$, $\beta = 11.1 \text{ mJ/mol K}^4$, and $\zeta = 0.0047 \text{ mJ/mol K}^6$ (see Fig. 3b). The value of the Sommerfeld coefficient (γ) is very close to zero, in agreement with the insulating ground state in this material. From the value of β , one can estimate the Debye temperature to be 141 K. The presence of the T^5 contribution indicates the existence of additional (besides acoustic, Debye interactions) low energy excitations to the heat capacity of $\text{Rb}_4\text{Ag}_2\text{BiBr}_9$. To describe the temperature variation of the specific heat of $\text{Rb}_4\text{Ag}_2\text{BiBr}_9$ in a wider temperature range, we used a **Debye model**.^{15,16} As can be seen from Fig. 3, although overall quite accurate ($R^2 = 0.9972$), the model fails to capture the $C_p(T)$ correctly, especially in the mid-temperature range (Θ_D derived from the fit is 145 K). To describe the temperature variation of the specific heat of $\text{Rb}_4\text{Ag}_2\text{BiBr}_9$ in a wider temperature range, **we extend the analysis to also include the optical contributions by using** $C_p(T) = (1-k)C_D(T) + kC_E(T)$, in which the lattice contribution to the specific heat is accounted for by both the Debye and Einstein integrals.¹⁴ The k parameter ensures the proper quantity of the oscillator modes involved.¹⁴ The least-squares fit ($R^2 = 0.99992$) of this expression to the experimental data (see solid blue line Fig. 3a) yields the following parameters: $\Theta_D = 168 \text{ K}$, $\Theta_E = 50 \text{ K}$, and $k = 0.24$. The Einstein term gives a relatively large contribution to

the total specific heat of $\text{Rb}_4\text{Ag}_2\text{BiBr}_9$ (cf. large value of k) and brings about a distinct maximum in the C_p/T^3 vs. T plot at a temperature $T_{\max} = 9$ K (see lower inset in Fig. 3a), which scales very well with the Einstein temperature, $\Theta_E \sim 5 \cdot T_{\max}$.¹⁵ **In order to unveil more details of the phonon structure in this material more studies are required such as inelastic neutron scattering experiments.**

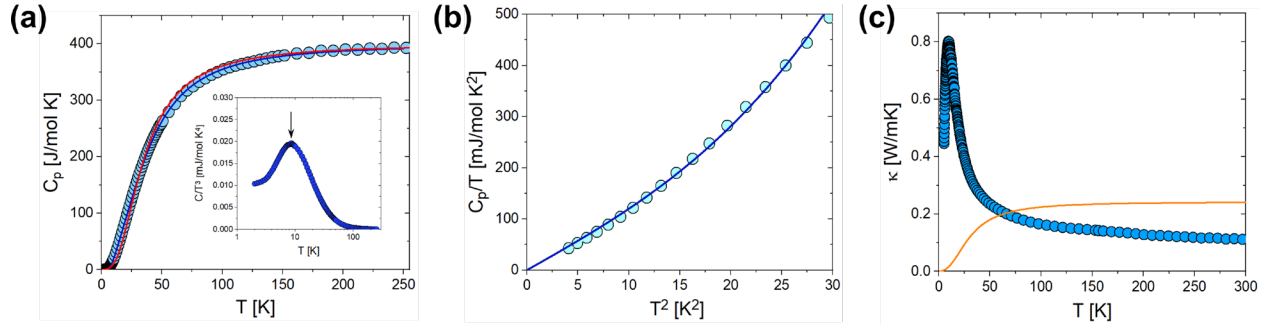


Figure 3. (a) Temperature dependence of the specific heat of a $\text{Rb}_4\text{Ag}_2\text{BiBr}_9$ SC. **The solid lines represent Debye (red line) and Debye-Einstein (blue) models (see text for more details).** The lower inset shows the specific heat data in the form of a C_p/T^3 vs. T plot. **(b) Low-temperature data of $\text{Rb}_4\text{Ag}_2\text{BiBr}_9$ as a C_p/T vs. T^2 function.** (c) Temperature dependence of the thermal conductivity of $\text{Rb}_4\text{Ag}_2\text{BiBr}_9$. The solid orange line presents the minimal phonon thermal conductivity.

Fig. 3c shows the temperature dependence of the thermal conductivity of $\text{Rb}_4\text{Ag}_2\text{BiBr}_9$, **measured along the ac plane.** The overall shape of $\kappa(T)$ is typical for non-magnetic insulators, **where lattice vibrations govern entirely the heat conduction.**¹⁷ At low temperatures, the thermal conductivity sharply increases with increasing temperature, forms a pronounced maximum at around 10 K, and then decreases moderately and reaches 0.1 W/mK at room temperature. This value is comparable with the lowest thermal conductivities reported in literature.¹⁸ In general, in non-magnetic, insulating crystals the maximum in $\kappa(T)$ occurs due to the reduction of the thermal scattering at low temperatures, i.e., in the regime where the phonon mean free path becomes larger than the interatomic distances. At higher temperatures, the phonon-phonon scattering dominates the thermal transport. It is worthwhile to compare the measured lattice thermal conductivity of $\text{Rb}_4\text{Ag}_2\text{BiBr}_9$ with the theoretically achievable minimal phonon contribution, (κ_L, min) . The latter may be calculated **using the Debye approximation following the model proposed by David Cahill and Robert Pohl,** in which no distinction is made between the transverse and longitudinal acoustic phonon modes.^{19,20} The results obtained for $\text{Rb}_4\text{Ag}_2\text{BiBr}_9$ (using $\Theta_D = 141$ K and numbers of atoms, $n = 2.95 \times 10^{28} \text{ m}^{-3}$) is shown in Fig. 3c by the solid line. As can be seen from Fig. 3c, the calculated (κ_L, min) is larger than the measured $\kappa(T)$, especially at higher temperatures, thus might indicate that some strong phonon-phonon processes might be involved in the reduction of $\kappa(T)$ in $\text{Rb}_4\text{Ag}_2\text{BiBr}_9$.

For radiation detection applications, the photon attenuation capability is crucial when energy discrimination is required, especially for resolving high-energy gamma-rays. Fig. 4a compares the photon attenuation capability of $\text{Rb}_4\text{Ag}_2\text{BiBr}_9$ with single element X-ray detector material silicon (Si), and

compound detector materials cadmium telluride (CdTe), 3D perovskite CsPbBr₃, and double perovskite Cs₂AgBiBr₆. Rb₄Ag₂BiBr₉ shows comparable attenuation capability for X-ray photons. The semiconductor bulk resistivity is a basic property that evaluates material's potential for reducing the detector leakage current, which serves as detector noise, and therefore, could degrade the detector energy resolution. The performed current-voltage (I-V) measurement for Rb₄Ag₂BiBr₉ SC (Fig. 4b) yields a high bulk crystal resistivity of $2.59 \times 10^9 \Omega \cdot \text{cm}$ (measured along the interlayer direction b axis), which is ideal for further exploring this material's potential for X-ray photon detection.

The defect density is another important figure of merit for evaluating semiconductor's potential for X-ray detection. Fig. 4c shows the space-charge-limited-current (SCLC) measurement for Rb₄Ag₂BiBr₉ SCs. The two transition regimes, namely Ohmic and trap-filled-limited (TFL), are observed. In the Ohmic regime, current is linearly proportional to the voltage, therefore the crystal's electrical resistivity could be evaluated from this region. In the TFL regime, all defect traps are filled by the injected charge carriers from the metal contacts, therefore, the density of trap states n_t could be estimated using the onset voltage V_{TFL} of the TFL regime according to the following formula,²¹

$$n_t = \frac{2\epsilon\epsilon_0}{eL^2} V_{\text{TFL}} \quad (1)$$

where ϵ (=14.07) is the dielectric constant, ϵ_0 is the vacuum permittivity, e is the electronic charge, and L is the crystal thickness. The density of trap states presenting in Rb₄Ag₂BiBr₉ SCs is estimated to be $3.33 \times 10^{10} \text{ cm}^{-3}$, which is comparable to that for MAPbBr₃ ($5.80 \times 10^9 \text{ cm}^{-3}$)²² and Cs₂AgBiBr₆ ($1.44 \times 10^{10} \text{ cm}^{-3}$)²³ double perovskites.

The detector operation stability serves an important role for X-ray detector development, especially when long-term detector operation is required. The Rb₄Ag₂BiBr₉-based X-ray detector stability was checked at a detector bias of +2 V (Fig. 4d). It is noticed that during the 30 seconds continuous detector operation, the detector current is relatively stable with no obvious drift, implying the 2D Rb₄Ag₂BiBr₉ may have much better long-term detector operation stability compared to the 3D halide perovskites such as Cs₂AgBiBr₆, MAPbI₃, and MAPbBr₃ (which are known to suffer from the halogen migration issues).^{2,24,25,26}

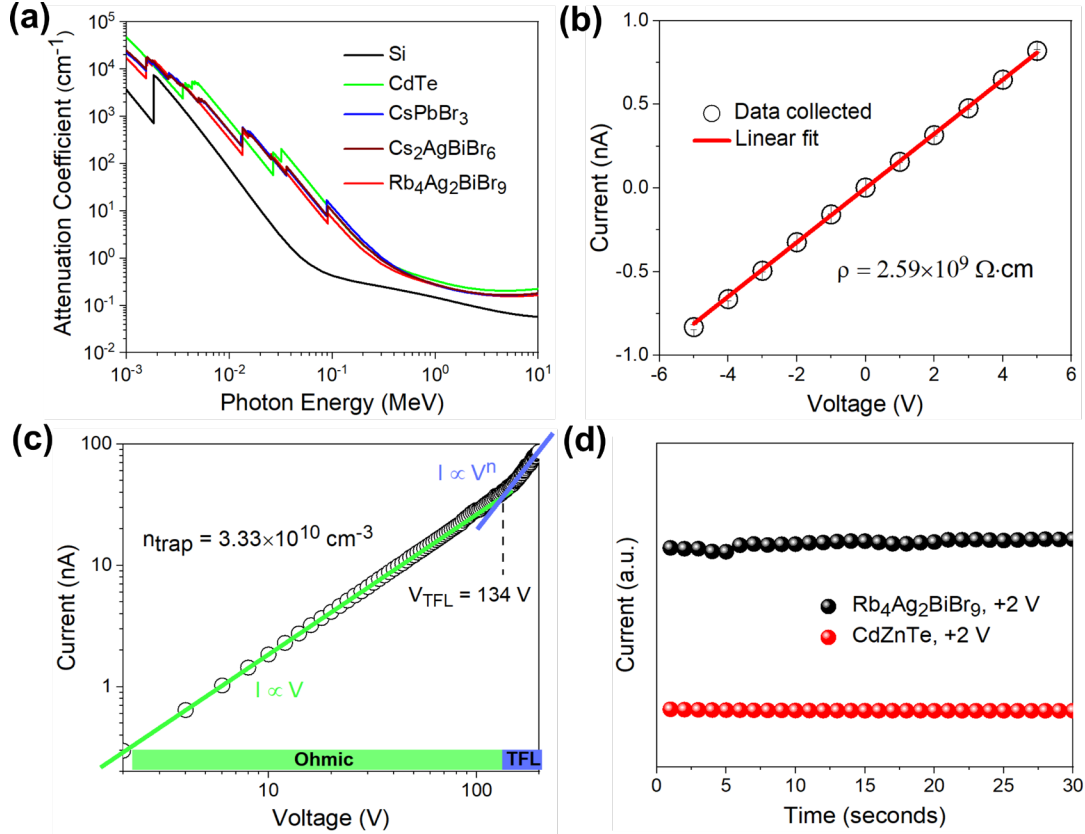


Figure 4. (a) Attenuation coefficient of Rb₄Ag₂BiBr₉ for photons compared to Si, CdTe, CsPbBr₃, and Cs₂AgBiBr₆, from soft X-ray to high-energy gamma-rays. (b) I-V measurement using Rb₄Ag₂BiBr₉ SCs, measurement was conducted at room temperature and under dark environment. (c) Measured SCLC curve for Rb₄Ag₂BiBr₉ SC. (d) Detector stability test at +2 V, compared to the CdZnTe detector at the same bias voltage.

Furthermore, we measured the charge carrier lifetime for Rb₄Ag₂BiBr₉ SC and powder samples (Fig. 5). The charge carrier lifetime is related to the carrier diffusion length through the equation $\lambda = \mu\tau E$ (where μ is the carrier mobility and E is the electric field). In general, long carrier lifetime is essential for enabling sufficient long carrier diffusion length. For Rb₄Ag₂BiBr₉ SCs, the intrinsic carrier lifetime is measured to be 2.9 ns, while the short 206 ps lifetime could be ascribed to the high level of defect traps on crystal surface, which leads to fast charge carrier recombination.¹⁰

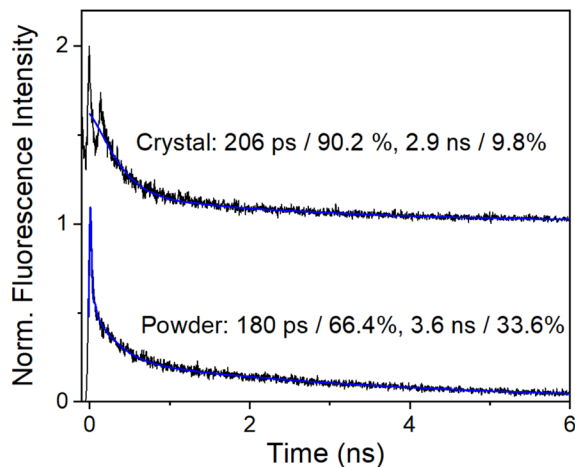


Figure 5. Charge carrier lifetime measurements on $\text{Rb}_4\text{Ag}_2\text{BiBr}_9$ SCs and powders using time-resolved fluorescence spectroscopy. The blue lines are the results of deconvolution fitting.

To evaluate the performance of $\text{Rb}_4\text{Ag}_2\text{BiBr}_9$ -based X-ray detectors (a schematic illustration for the fabricated $\text{Rb}_4\text{Ag}_2\text{BiBr}_9$ -based X-ray detector is shown in Fig. 6a), we first conducted the ‘on’ and ‘off’ measurements (Fig. 6b) to demonstrate the sensitive response of $\text{Rb}_4\text{Ag}_2\text{BiBr}_9$ to X-ray irradiation. The significant increase of current when X-ray beam is turned on implies that $\text{Rb}_4\text{Ag}_2\text{BiBr}_9$ SCs are highly responsive to soft 8 keV X-rays. Moreover, by varying the X-ray tube current, which corresponds to different dose rate, we determined the $\text{Rb}_4\text{Ag}_2\text{BiBr}_9$ -based X-ray detector sensitivity to be $29.7 \text{ uCGy}^{-1}\text{cm}^{-2}$ (at a low electric field of $E = 4 \text{ V/mm}$, Fig. 6c). Despite the fact that the determined detector sensitivity for $\text{Rb}_4\text{Ag}_2\text{BiBr}_9$ is much lower compared to that of the 3D halide perovskites MAPbI_3 ($1471.7 \text{ uCGy}^{-1}\text{cm}^{-2}$ at $E = 3.3 \text{ V/mm}$)²⁷ and FAPbBr_3 ($130 \text{ uCGy}^{-1}\text{cm}^{-2}$ at $E = 0.5 \text{ V/mm}$)²⁸ (see Table 1 for a comparison of the detector sensitivity), the better long-term operation stability of 2D perovskites is a major advantage warranting further exploration of this material. In addition, we note that the detector sensitivity could be further enhanced dramatically to $222.03 \text{ uCGy}^{-1}\text{cm}^{-2}$ when the detector is operated at +60 V (Fig. 6d and 6e), which corresponds to electric field $E = 24 \text{ V/mm}$. Finally, it should be stressed that the detector sensitivity measured here for $\text{Rb}_4\text{Ag}_2\text{BiBr}_9$ is even better than the previous reports of detector sensitivity for the 3D double perovskite $\text{Cs}_2\text{AgBiBr}_6$ at the same electric field ($105 \text{ uCGy}^{-1}\text{cm}^{-2}$ at $E = 25 \text{ V/mm}$).²⁹

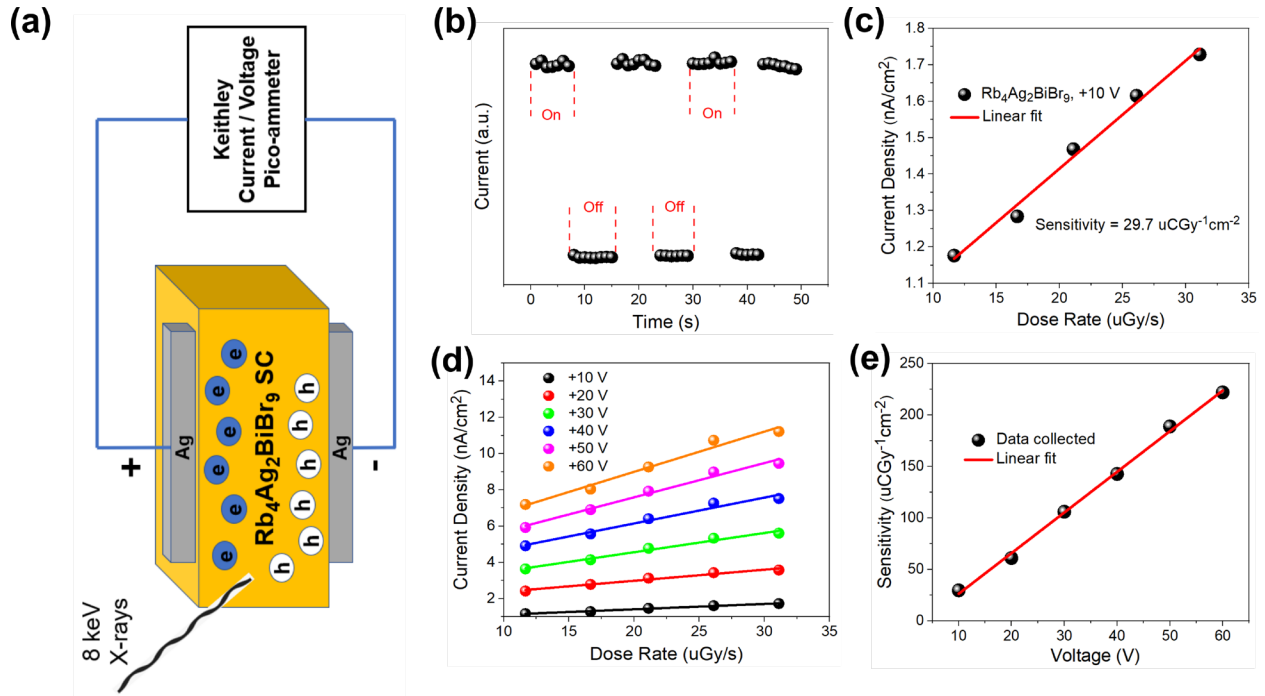


Figure 6. (a) A schematic illustration of the $\text{Rb}_4\text{Ag}_2\text{BiBr}_9$ -based X-ray detectors fabricated in this work. (b) Response of the $\text{Rb}_4\text{Ag}_2\text{BiBr}_9$ -based detector to soft X-rays produced from a Cu X-ray tube. (c) Current density vs. dose rate measurement for determining the X-ray detector sensitivity. (d) Measured detector current density vs. dose rate for extracting the detector sensitivity at different bias voltages. (e) Plot of the detector sensitivity vs. detector bias, from 10 V to 60 V.

Table 1. A comparison of the detector sensitivity determined for $\text{Rb}_4\text{Ag}_2\text{BiBr}_9$ with the reported sensitivity values for the related 3D and 2D halide perovskite SCs.

Material	Dimensionality	X-Ray Tube Anode	Electric Field (V/mm)	Detector Sensitivity ($\mu\text{CGy}^{-1}\text{cm}^{-2}$)	Reference
$\text{Cs}_2\text{AgBiBr}_6$	3D	Tungsten (W)	25	105	29
MAPbBr_3	3D	W	5	529	30
MAPbI_3	3D	W	3.3	1471.7	27
FAPbBr_3	3D	W	0.5	130	28
CsPbBr_3	3D	W	-	4086	34
$\text{FA}_{0.85}\text{MA}_{0.1}\text{Cs}_{0.05}\text{PbI}_{2.55}\text{Br}_{0.45}$	3D	W	-	$(3.5 \pm 0.2) \times 10^6$	33
$(\text{BA})_2\text{CsPb}_2\text{Br}_7$	2D	-	2.53	13260	31
BDAPbI_4 (BDA= $\text{NH}_3\text{C}_4\text{H}_8\text{NH}_3$)	2D	-	310	242	32

Rb ₄ Ag ₂ BiBr ₉	2D	Cu	24	222.03	This work
---	----	----	----	--------	-----------

■ CONCLUSIONS

In summary, we optimized the crystal growth methodology for producing Rb₄Ag₂BiBr₉ SCs. It was found that best quality Rb₄Ag₂BiBr₉ SCs can be realized by adopting the slow cooling of a hot aqueous hydrobromic acid solution at 130 °C. The solution-processed Rb₄Ag₂BiBr₉ SCs are found to have an ideal semiconductor resistivity of $2.59 \times 10^9 \Omega \cdot \text{cm}$ and the fabricated Rb₄Ag₂BiBr₉-based X-ray detector shows desirable good long-term operation stability, which render Rb₄Ag₂BiBr₉ as promising candidates for the use as one of the next-generation low-cost X-ray detector materials. Moreover, the absence of structural phase transitions for Rb₄Ag₂BiBr₉ is further confirmed by the heat capacity measurements. The fabricated X-ray detector made of a Rb₄Ag₂BiBr₉ SC shows a detector sensitivity of 222.03 $\mu\text{CGy}^{-1}\text{cm}^{-2}$ at an electric field of 24 V/mm. In addition to these performance metrics, the low cost, ease of preparation, high stability and earth-abundant chemical compositions make Rb₄Ag₂BiBr₉ an attractive X-ray detector material candidate for further studies. Future work should be focused on reducing the intrinsic defect density to enhance the X-ray detector performance and doping to enhance the charge carrier transport properties. In addition to the potential practical applications, our results further suggest remarkably low thermal conductivity of Rb₄Ag₂BiBr₉, which is comparable with the lowest thermal conductivities reported in literature. In fact, the measured thermal conductivities at temperatures above 100 K are lower than the minimal phonon thermal conductivity calculated using the Debye model. Therefore, more fundamental studies on Rb₄Ag₂BiBr₉ are warranted to better understand the lattice dynamics of this material.

■ CONFLICTS OF INTEREST

The authors declare no competing financial interest.

■ ACKNOWLEDGEMENTS

This material is based upon work supported by the U.S. Department of Energy, Office of Science, Office of Basic Energy Sciences, under the award number DE-SC0021158. X-ray response tests were conducted at the X-ray lab located at the Biomolecular Structure Core (BSC)-Norman, University of Oklahoma, which is supported in part by an Institutional Development Award (IDeA) from the National Institute of General Medical Sciences of the National Institutes of Health (Award P20GM103640), the National Science Foundation (Award 0922269), and the University of Oklahoma Department of Chemistry and Biochemistry. K.G. acknowledges support from the US DOE BES Energy Frontier Research Centre “Thermal Energy Transport under Irradiation” (TETI). Y.-Z. Ma acknowledges support from the

Laboratory Directed Research and Development Program of Oak Ridge National Laboratory, managed by UT-Battelle, LLC, for the US Department of Energy.

■ REFERENCES

- 1 Bavdaz, M.; Peacock, A.; Owens, A. Future Space Applications of Compound Semiconductor X-Ray Detectors. *Nucl. Instruments Methods Phys. Res. Sect. A Accel. Spectrometers, Detect. Assoc. Equip.* **2001**, *458* (1–2), 123–131.
- 2 Zhang, Z.; Cao, D.; Huang, Z.; Danilov, E. O.; Chung, C. C.; Sun, D.; Yang, G. Gamma-Ray Detection Using Bi-Poor Cs₂AgBiBr₆ Double Perovskite Single Crystals. *Adv. Opt. Mater.* **2021**, *9* (8), 2001575.
- 3 Zhang, Z.; Saparov, B. Charge Carrier Mobility of Halide Perovskite Single Crystals for Ionizing Radiation Detection. *Appl. Phys. Lett.* **2021**, *119* (3), 030502.
- 4 Zha, G. Q.; Xiang, H.; Liu, T.; Xu, Y. D.; Wang, T.; Jie, W. Q. The Analysis of X-Ray Response of CdZnTe Detectors. *Sci. China Technol. Sci.* **2012**, *55* (8), 2295–2299.
- 5 Lioliou, G.; Whitaker, M. D. C.; Barnett, A. M. High Temperature GaAs X-Ray Detectors. *J. Appl. Phys.* **2017**, *122* (24), 244506.
- 6 Hitomi, K.; Muroi, O.; Matsumoto, M.; Hirabuki, R.; Shoji, T.; Hiratate, Y. X-Ray Detection Characteristics of Thallium Bromide Nuclear Radiation Detectors. *IEEE Trans. Nucl. Sci.* **2000**, *47* (3 PART 2), 777–779.
- 7 Koch-Mehrin, K. A. L.; Bugby, S. L.; Lees, J. E.; Veale, M. C.; Wilson, M. D. Charge Sharing and Charge Loss in High-Flux Capable Pixelated CdZnTe Detectors. *Sensors* **2021**, *21* (9), 3260.
- 8 Datta, A.; Fiala, J.; Becla, P.; Motakef, S. Stable Room-Temperature Thallium Bromide Semiconductor Radiation Detectors. *APL Mater.* **2017**, *5* (10), 106109.
- 9 Eperon, G. E.; Stranks, S. D.; Menelaou, C.; Johnston, M. B.; Herz, L. M.; Snaith, H. J. Formamidinium Lead Trihalide: A Broadly Tunable Perovskite for Efficient Planar Heterojunction Solar Cells. *Energy Environ. Sci.* **2014**, *7* (3), 982–988.
- 10 Han, Q.; Bae, S. H.; Sun, P.; Hsieh, Y. T.; Yang, Y.; Rim, Y. S.; Zhao, H.; Chen, Q.; Shi, W.; Li, G.; Yeng, Y. Single Crystal Formamidinium Lead Iodide (FAPbI₃): Insight into the Structural, Optical, and Electrical Properties. *Adv. Mater.* **2016**, *28* (11), 2253–2258.
- 11 Tsai, H.; Liu, F.; Shrestha, S.; Fernando, K.; Tretiak, S.; Scott, B.; Vo, D. T.; Strzalka, J.; Nie, W. A Sensitive and Robust Thin-Film x-Ray Detector Using 2D Layered Perovskite Diodes. *Sci. Adv.* **2020**, *6* (15).
- 12 Zheng, X.; Zhao, W.; Wang, P.; Tan, H.; Saidaminov, M. I.; Tie, S.; Chen, L.; Peng, Y.; Long, J.; Zhang, W. H. Ultrasensitive and Stable X-Ray Detection Using Zero-Dimensional Lead-Free Perovskites. *J. Energy Chem.* **2020**, *49*, 299–306.

- 13 Sharma, M.; Yangui, A.; Whiteside, V. R.; Sellers, I. R.; Han, D.; Chen, S.; Du, M. H.; Saparov, B. Rb 4 Ag 2 BiBr 9 : A Lead-Free Visible Light Absorbing Halide Semiconductor with Improved Stability. *Inorg. Chem.* **2019**, *58* (7), 4446–4455.
- 14 Fraga, G. L. F.; Brandão, D. E.; Sereni, J. G. Specific Heat of X₂MnSn (X = Co, Ni, Pd, Cu), X₂MnIn (X = Ni, Pd) and Ni₂MnSb Heusler Compounds. *J. Magn. Magn. Mater.* **1991**, *102* (1–2), 199–207.
- 15 Tari, A. *The Specific Heat of Matter at Low Temperatures*, Imperial College Press, London, 2003.
- 16 Debye, P. *Zur Theorie Der Spezifischen Wärmen.* *Ann. Phys.* **1912**, *344* (14), 789–839.
- 17 Tritt, T. M. *Thermal Conductivity Theory, Properties, and Applications*, Springer, 2012.
- 18 Gibson, Q. D.; Zhao, T.; Daniels, L. M.; Walker, H. C.; Daou, R.; Hébert, S.; Zanella, M.; Dyer, M. S.; Claridge, J. B.; Slater, B.; Gaultois, M. W.; Corà, F.; Alaria, J.; Rosseinsky, M. J. Low Thermal Conductivity in a Modular Inorganic Material with Bonding Anisotropy and Mismatch. *Science (80-.)*. **2021**, eabh1619.
- 19 Giannò, K.; Sologubenko, A.; Chernikov, M.; Ott, H.; Fisher, I.; Canfield, P. Low-Temperature Thermal Conductivity of a Single-Grain Y-Mg-Zn Icosahedral Quasicrystal. *Phys. Rev. B - Condens. Matter Mater. Phys.* **2000**, *62* (1), 292–300.
- 20 Cahill, D. G.; Pohl, R. O. Heat Flow and Lattice Vibrations in Glasses. *Solid State Commun.* **1989**, *70* (10), 927–930.
- 21 Bube, R. H. Trap Density Determination by Space-Charge-Limited Currents. *J. Appl. Phys.* **1962**, *33* (5), 1733–1737.
- 22 Shi, D.; Adinolfi, V.; Comin, R.; Yuan, M.; Alarousu, E.; Buin, A.; Chen, Y.; Hoogland, S.; Rothenberger, A.; Katsiev, K.; Losovyj, Y.; Zhang, X.; Dowben, P. A.; Mohammed, O. F.; Sargent, E. H.; Bakr, O. M. Low Trap-State Density and Long Carrier Diffusion in Organolead Trihalide Perovskite Single Crystals. *Science (80-.)*. **2015**, *347* (6221), 519–522.
- 23 Zhang, Z.; Chung, C. C.; Huang, Z.; Vetter, E.; Seyitliyev, D.; Sun, D.; Gundogdu, K.; Castellano, F. N.; Danilov, E. O.; Yang, G. Towards Radiation Detection Using Cs₂AgBiBr₆ Double Perovskite Single Crystals. *Mater. Lett.* **2020**, *269*, 127667.
- 24 Yakunin, S.; Dirin, D. N.; Shynkarenko, Y.; Morad, V.; Cherniukh, I.; Nazarenko, O.; Kreil, D.; Nauser, T.; Kovalenko, M. V. Detection of Gamma Photons Using Solution-Grown Single Crystals of Hybrid Lead Halide Perovskites. *Nat. Photonics* **2016**, *10* (9), 585–589.
- 25 Futscher, M. H.; Lee, J. M.; McGovern, L.; Muscarella, L. A.; Wang, T.; Haider, M. I.; Fakharuddin, A.; Schmidt-Mende, L.; Ehrler, B. Quantification of Ion Migration in CH₃NH₃PbI₃ Perovskite Solar Cells by Transient Capacitance Measurements. *Mater. Horizons* **2019**, *6* (7), 1497–1503.
- 26 Oranskaia, A.; Yin, J.; Bakr, O. M.; Brédas, J. L.; Mohammed, O. F. Halogen Migration in Hybrid Perovskites: The Organic Cation Matters. *J. Phys. Chem. Lett.* **2018**, *9* (18), 5474–5480.

- 27 Geng, X.; Zhang, H.; Ren, J.; He, P.; Zhang, P.; Feng, Q.; Pan, K.; Dun, G.; Wang, F.; Zheng, X.; Tian, H.; Xie, D.; Yang, Y.; Ren, T. L. High-Performance Single Crystal $\text{CH}_3\text{NH}_3\text{PbI}_3$ perovskite x-Ray Detector. *Appl. Phys. Lett.* **2021**, *118* (6), 063506.
- 28 Yao, M.; Jiang, J.; Xin, D.; Ma, Y.; Wei, W.; Zheng, X.; Shen, L. High-Temperature Stable FAPbBr_3 Single Crystals for Sensitive X-Ray and Visible Light Detection toward Space. *Nano Lett.* **2021**, *21* (9), 3947–3955.
- 29 Pan, W.; Wu, H.; Luo, J.; Deng, Z.; Ge, C.; Chen, C.; Jiang, X.; Yin, W. J.; Niu, G.; Zhu, L.; Yin, L.; Zhou, Y.; Xie, Q.; Ke, X.; Sui, M.; Tang, J. $\text{Cs}_2\text{AgBiBr}_6$ Single-Crystal X-Ray Detectors with a Low Detection Limit. *Nat. Photonics* **2017**, *11* (11), 726–732.
- 30 Li, L.; Liu, X.; Zhang, H.; Zhang, B.; Jie, W.; Sellin, P. J.; Hu, C.; Zeng, G.; Xu, Y. Enhanced X-Ray Sensitivity of MAPbBr_3 Detector by Tailoring the Interface-States Density. *ACS Appl. Mater. Interfaces* **2019**, *11* (7), 7522–7528.
- 31 Xiao, B.; Sun, Q.; Wang, F.; Wang, S.; Zhang, B. Bin; Wang, J.; Jie, W.; Sellin, P.; Xu, Y. Towards Superior X-Ray Detection Performance of Two-Dimensional Halide Perovskite Crystals by Adjusting the Anisotropic Transport Behavior. *J. Mater. Chem. A* **2021**, *9* (22), 13209–13219.
- 32 Shen, Y.; Liu, Y.; Ye, H.; Zheng, Y.; Wei, Q.; Xia, Y.; Chen, Y.; Zhao, K.; Huang, W.; Liu, S. (Frank). Centimeter-Sized Single Crystal of Two-Dimensional Halide Perovskites Incorporating Straight-Chain Symmetric Diammonium Ion for X-Ray Detection. *Angew. Chemie* **2020**, *132* (35), 15006–15012.
- 33 Liu, Y.; Zhang, Y.; Zhu, X.; Feng, J.; Spanopoulos, I.; Ke, W.; He, Y.; Ren, X.; Yang, Z.; Xiao, F.; Zhao, K.; Kanatzidis, M.; Liu, S. Triple-Cation and Mixed-Halide Perovskite Single Crystal for High-Performance X-Ray Imaging. *Adv. Mater.* **2021**, *33* (8), 2006010.
- 34 Peng, J.; Xia, C. Q.; Xu, Y.; Li, R.; Cui, L.; Clegg, J. K.; Herz, L. M.; Johnston, M. B.; Lin, Q. Crystallization of CsPbBr_3 Single Crystals in Water for X-Ray Detection. *Nat. Commun.* **2021**, *12* (1), 1–10.